Fuel 234 (2018) 199–206

Contents lists available at ScienceDirect

Fuel

journal homepage: www.elsevier.com/locate/fuel

Full Length Article

Kinetic modeling of soot formation in premixed burner-stabilized stagnation ethylene flames at heavily sooting condition

Warumporn Pejpichestakul[a,b], Alessio Frassoldati[a], Alessandro Parente[b,c], Tiziano Faravelli[a,*]

[a] Department of Chemistry, Materials and Chemical Engineering "G. Natta", Politecnico di Milano, P.zza Leonardo da Vinci 32, 20133 Milano, Italy
[b] Université Libre de Bruxelles, Ecole polytechnique de Bruxelles, Aero-Thermo-Mechanics Laboratory, Avenue F.D Roosevelt, 50 – CP 165/41, 1050 Brussels, Belgium
[c] Université Libre de Bruxelles and Vrije Universiteit Brussel, Combustion and Robust Optimization Group (BURN), Bruxelles, Belgium

ARTICLE INFO

Keywords:
Soot
Laminar premixed flame
Particle size distribution functions
Kinetic modeling

ABSTRACT

A detailed kinetic mechanism of soot formation and oxidation is revised and extended to include temperature-dependent collision efficiencies. The collision efficiency for various particle size is studied and compared with experimental data and molecular dynamics simulations for the PAH dimerization where the experimental data are not available. This revised kinetic model is validated in comparison with the premixed burner-stabilized stagnation ethylene flames at heavily sooting conditions. The results showed that quasi-one-dimensional numerical simulations can capture the flame structure and predict soot formation quite satisfactorily. The predicted particle size distribution function (PSDF) is in reasonable agreement with experimental results, but the model only partially reproduces the distinct separation between nucleation and coagulation modes observed experimentally. This leads to some discrepancies in the prediction of soot number density, while the predicted soot volume fraction, which is dominated by the large particles of the PSDF, is in generally good agreement with the experimental data. There is an overestimation of the initial soot volume fraction in the flame region close to the burner, which is a consequence of the over-prediction of the amount of young particles. Therefore, the prediction of PAHs formation and their condensation on soot, which controls the nucleation rate, will require further attention. The comparison between the temperature-dependent model and the model neglecting the temperature dependency showed that the temperature-dependent model could improve the prediction of soot number density, which is controlled by small particles.

1. Introduction

Soot is made of carbonaceous nanoparticles formed from combustion processes which can be emitted directly to the atmosphere. Soot formation in practical applications influences the radiative heat losses and lowers the efficiency of combustors [1]. Furthermore, soot particles adversely affect health and the environment [1]. Consequently, they are considered as a primary pollutant source [2]. Nowadays, legislation is becoming more restrictive for particulate emission, i.e. the EU air quality directive defines the $PM_{2.5}$ concentration of 25 $\mu g/m^3$ on an annual basis and will lower a threshold to 20 $\mu g/m^3$ by 2020 [2]. Therefore, there is a need to understand the fundamental mechanism of soot formation to reduce its emission.

It is widely accepted that polycyclic aromatic hydrocarbons (PAH) are the soot precursor species. Gas-phase aliphatic species form polycyclic aromatic hydrocarbon (PAH) through several processes. The most well-known surface growth sequential pathway is hydrogen abstraction and acetylene addition (HACA) mechanisms proposed by [3,4]. The other surface growth pathway which plays a major role in soot formation is the recombination of odd-carbon atom radicals such as allyl, propargyl, cyclopentadienyl, and indenyl [5–9]. The other possible pathway that involves acetylene specifically at the zig-zag edges of PAH is carbon addition and hydrogen migration (CAHM) proposed by [10]. This proposed pathway was introduced to explain the soot formation in conditions where the presence of H atoms is insufficient to sustain the HACA mechanism.

PAHs can interact and form stacked structures that eventually lead to the formation of soot nuclei through physical and chemical reactions [11]. The soot nucleation by physical interactions or the PAH dimerization is possible in the flame only for large PAHs in the area of 50 carbon atoms, which can form durable Van de Waals interaction forces [8]. The other reaction is chemical coalescence through localized π-electronic states of PAH radicals. Both physical and chemical pathways leading to the formation of soot nuclei are included in recent soot

* Corresponding author.
E-mail address: tiziano.faravelli@polimi.it (T. Faravelli).

https://doi.org/10.1016/j.fuel.2018.07.022
Received 7 December 2017; Received in revised form 9 May 2018; Accepted 4 July 2018
Available online 11 July 2018

models [12,13]. The collision of nascent soot particles leads to the formation of larger soot primary particles [14]. The coagulation of heavy PAHs and small soot particles can also form particles whose size is up to 10–40 nm, called primary particles [15,16]. The coagulation is an important process that controls the particle size distribution function (PSDF) of the soot particles. Additionally, the surface growth reactions also significantly contribute to the soot growth in the flame through the well-known HACA mechanism together with the condensation of gaseous species and PAH [3,4].

The evidence from experimental studies is not sufficient to fully describe the PAH dimerization and the coagulation of soot particles, particularly at typical flame temperatures. Theoretical calculations by Wang (2011) [11] demonstrated that the entropy effect that leads the dimerization of PAH cannot be relevant at flame temperatures. D'Alessio et al. [17] studied the deposition of soot nanoparticles from premixed ethylene-air flames on a mica plate by atomic force microscopy technique (AFM). They observed very low collision efficiencies for small particles and in general a strong size-dependency. In fact, the collision frequency is intrinsically proportional to particle size. However, several soot models considered constant collision efficiencies [18–20]. D'Alessio et al. [17] suggested a temperature-dependent model for collision efficiency, which has been recently confirmed by experimental studies [21]. The dependence of collision efficiency with temperature is associated with the competition between thermal rebound effects and the Van der Waals forces [17]. Molecular dynamics simulations (MD) of the collision of monomers revealed that there is an increase of the collision efficiencies with the colliding monomer mass [14,15], while the collision efficiencies are inversely related to temperature. However, these theoretical studies were performed up to a maximum temperature of 1500 K, which is approximately at the lower limit of soot threshold temperature of ethylene flames [24].

Soot formation in laminar premixed flames of ethylene has been extensively studied by different authors. In particular, in this work, we refer to the ethylene premixed flames measured using the burner-stabilized stagnation (BSS) flame approach proposed by Wang and coworkers [25,26]. This technique minimizes the effect of probe-perturbation in soot sampling, while the HR-DMA analysis provides the detailed information of PSDF. The recent BSS flames from Gu et al. [27], who studied heavily and lightly sooting conditions, are also investigated. By changing the inlet cold gas velocity, they obtained different maximum flame temperatures. These experimental data, always referring to the same fuel, thus provide the broad range of sooting conditions needed to understand the processes leading to soot formation and in particular the temperature effects.

In this work, a detailed kinetic modeling of premixed BSS ethylene flames has been performed to study the soot formation with temperature dependency, with particular attention to collision efficiencies. In particular, we compared the model proposed by D'Alessio et al. [17], which takes into account the effect of colliding particle size and temperature, with the MD simulations [22,23] of large PAH dimerization. This analysis allowed to better characterize the effect of colliding particle sizes and temperature on the collision efficiencies. A revised soot model was developed and validated in comparison with experimental data in a wide range of conditions using BSS flames. The comparison between experimental and model results includes temperature profiles, PSDFs of soot particles, number densities, and soot volume fractions.

2. Model description

A discrete sectional method is used to model the soot formation and evolution from the gas-to-particle process by the discretization of the particle size spectrum into a limited number of lumped-pseudo species named BINs. This model uses a multi-sectional approach that discretizes the number of carbon atoms into 25 sections with a discretization space of two, and three different hydrogenation levels, denoted from A to C. Table 1 summarizes the classes of lumped pseudo-species (BINs) and their properties. The comparison between H/C ratio defined for each subclass and molecular weight is shown in Fig. 1. The first four BINs are the heavy PAHs which are formed by the gas-phase reactions, while BINs larger than BIN4 constitute the soot particles. The smallest soot particle is BIN5, with a size of about 2 nm. Recent experimental observations suggest to consider smaller soot particles [28]. Anyway, the reduction of the first soot particle diameter does not significantly affect both the soot volume fraction and the PSDF. BIN12 represents primary particles with a size of about 10 nm, which further constitutes fractal aggregates (BIN13–BIN25). The spherical shape with a constant density of 1500 kg/m^3 is assumed for soot particles (BIN5-12), while the fractal dimension of 1.8 is assumed for soot aggregates. This soot model is developed based on the previous soot kinetic mechanism proposed by Saggese et al. [29]. Differences with the previous model are mostly related to the number of BINs and the coagulation efficiencies discussed in this paper.

Table 1
Properties of lumped pseudo-species.

BIN$_i$	nC	Molecular Mass (amu)	Equivalent Spherical Diameter (nm)	H/C ratio		
				A	B	C
Heavy PAHs						
BIN1	20	~250	0.81	0.8	0.5	0.2
BIN2	40	~500	1.02	0.775	0.4	0.2
BIN3	80	~1000	1.28	0.75	0.3	0.1
BIN4	160	~2000	1.60	0.725	0.2	0.05
Soot particles						
BIN5	320	~4×10^3	2.02	0.7	0.2	0.05
BIN6	640	~8×10^3	2.55	0.675	0.2	0.05
BIN7	1.25×10^3	~1.55×10^4	3.18	0.65	0.2	0.05
BIN8	2.5×10^3	~3×10^4	4.01	0.625	0.2	0.05
BIN9	5×10^3	~6×10^4	5.05	0.6	0.2	0.05
BIN10	1×10^4	~1.2×10^5	6.37	0.575	0.2	0.05
BIN11	2×10^4	~2.45×10^5	8.02	0.55	0.2	0.05
BIN12	4×10^4	~4.9×10^5	10.11	0.525	0.2	0.05
Soot aggregates						
BIN13	8×10^4	~9.7×10^5	12.73	0.5	0.2	0.05
BIN14	1.6×10^5	~1.95×10^6	16.04	0.475	0.2	0.05
BIN15	3.2×10^5	~3.9×10^6	20.21	0.45	0.2	0.05
BIN16	6.4×10^5	~7.8×10^6	25.47	0.425	0.2	0.05
BIN17	1.25×10^6	~1.51×10^7	31.83	0.4	0.2	0.05
BIN18	2.5×10^6	~3.02×10^7	40.11	0.375	0.2	0.05
BIN19	5×10^6	~6.02×10^7	50.53	0.35	0.2	0.05
BIN20	1×10^7	~1.21×10^8	63.66	0.325	0.2	0.05
BIN21	2×10^7	~2.41×10^8	80.21	0.3	0.2	0.05
BIN22	4×10^7	~4.82×10^8	101.06	0.3	0.2	0.05
BIN23	8×10^7	~9.64×10^8	127.33	0.3	0.2	0.05
BIN24	1.6×10^8	~1.93×10^9	160.42	0.3	0.2	0.05
BIN25	3.2×10^8	~3.86×10^9	202.12	0.3	0.2	0.05

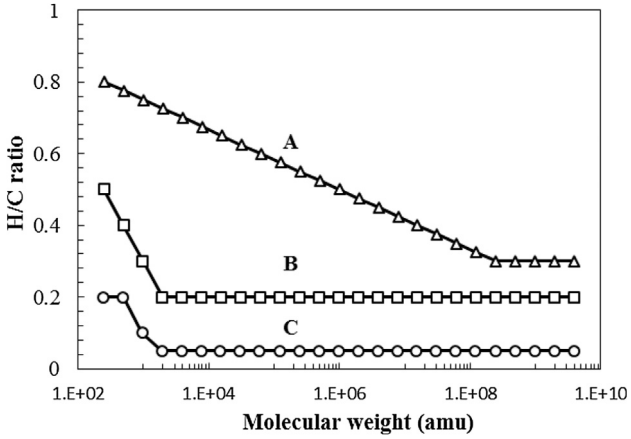

Fig. 1. Comparison between H/C ratio assigned to each BIN.

Table 2
Flame conditions of premixed ethylene BSS flames [27].

Flame	Mole fractions			Cold gas velocity (cm/s)	Temp. at burner (K)	Temp. at stagnation plate (K)	Max temp. (K)
	C_2H_4	O_2	Ar				
L1	0.136	0.164	0.7	4.5	383 ± 20	396 ± 10	1559 ± 61
L2	0.136	0.164	0.7	5.5	371 ± 20	393 ± 10	1622 ± 66
L3	0.136	0.164	0.7	6.5	399 ± 20	393 ± 10	1654 ± 66
L4	0.136	0.164	0.7	7.5	503 ± 20	397 ± 10	1713 ± 72

The soot sub-mechanism is coupled to the elementary mechanism that includes the reactions of gas-phase species up to PAH (from C_1-C_{16}) using POLIMI1602 kinetic mechanism [30,31]. The complete soot mechanism consists of ~350 species and over 20,000 reactions.

The gas-phase kinetic mechanism is able to describe the formation of PAHs up to pyrene. All numerical simulations were performed using OpenSMOKE++ code [32]. The numerical simulation exploits quasi-one-dimensional computational model for the premixed BSS ethylene flames with a treatment of the stagnation plane as a non-slip boundary condition with the temperature measured in the experiment on the stagnation plate. Heat losses due to radiative heat transfer are calculated using the optically thin approximation and the emissivity of gaseous species and soot particles [33,34]. The sheath gas temperature is considered as identical to the temperature at burner surface as suggested by the experiment [27]. The comparison with laminar premixed ethylene-oxygen-argon flames in heavily sooting conditions ($\phi = 2.5$) from [27] is also presented in this work. The soot distributions and its properties are taken from the spatial shift location to account for the probe-induced effect in the soot sample [35].

The flames conditions investigated in this paper are summarized in Table 2.

3. Comparison of collision efficiency

This Section compares the collision efficiency of PAH dimerization calculated from numerical simulations by Totton et al. [23] and Chung et al. [22], and the temperature and size dependent collision efficiency proposed by D'Alessio et al. [17] (Eq. (1)). The collision efficiency (γ) is the probability that colliding particles will stick and coagulate.

$$\gamma = 1 - \left(1 + \frac{\Phi_0}{k_b T}\right) \exp\left(-\frac{\Phi_0}{k_b T}\right) \tag{1}$$

where Φ_0 is the potential well depth, k_b is the Boltzmann constant and T is temperature. The potential well depth is calculated by Eq. (2) [36].

$$\Phi_0 = \frac{A}{6}\left\{\frac{2R_1R_2}{(2R_1 + 2R_2 + D)D} + \frac{2R_1R_2}{(2R_1 + D)(2R_2 + D)} + \ln\frac{(2R_1 + 2R_2 + D)D}{(2R_1 + D)(2R_1 + D)}\right\} \tag{2}$$

where A is Hamaker constant, R_1 and R_2 are radii of colliding entities, and D is the separation distance.

As the potential well depth is related to the separation distance, it is necessary to evaluate the separation distance for heavy PAHs. In this work, we obtained D on the basis of the results of MD simulations of PAH dimerization [22,23] and the equations presented above. The diameter of PAH is calculated as $d_{PAH} = d_A\sqrt{\frac{2nC}{3}}$, where d_A denotes the size of a single aromatic ring which equals to $1.395\sqrt{3}$ Ångström and nC is the number of carbon atoms [37]. The Hamaker constant of each PAH is obtained from an interpolation based on the H/C ratio, and ranges from 3E − 20 J of benzene (H/C = 1) to 5E − 19 J of graphite (H/C = 0), and has a value of 5E − 20 J for H/C = 0.5 [13]. Fig. 2 shows the separation distances at different temperatures and colliding particles sizes. It is possible to observe that, despite some uncertainties, D is mainly in the range between 0.1 and 0.4 nm. The average separation distance of 0.21 nm is therefore selected for the collision of colliding particles less than 2 nm. Fig. 3 shows the collision efficiencies of different peri-condensed aromatic hydrocarbons (PCAH) as a function of temperature. The calculated collision efficiency obtained using a separation distance of 0.21 nm is in agreement with the calculation from MD results [22,23], in particular at high temperature. At 1500 K, the collision efficiency calculated using MD is quite low, as depicted in Fig. 3a, where it approaches zero for pyrene and coronene. These quite low values are explained on the basis of insufficiently long trajectories to capture the successive dimerization [23]. However, overpredictions of calculated collision efficiency using a separation distance of 0.21 nm in all temperatures are observed for circumcoronene ($C_{54}H_{18}$) in Fig. 3a, suggesting that the separation distance increases with the particle size. The comparison with MD results shows that, despite uncertainties and simplifications, the model adopted in the present work is able to evaluate not only the absolute value of the collision efficiency but also the effect of the size of colliding entities and temperature. However, it is worth noting that the calculated collision efficiency is underestimated at low temperatures.

To better understand the collision efficiency of the larger colliding entities, Fig. 4 shows the comparison with the experimental data of D'Alessio et al. [17]. This experimental data set provides the collision efficiency between a mica plate and solid nanoparticles. In order to compare its interaction with the particles, it is reasonable to assume the mica plate as micron-sized agglomerate with the Hamaker constant of mica material which is 1E − 19 J [36]. The separation distance of the homo-molecular particle interaction is obtained from the interpolation between the separation distances of PAH and the micron-sized agglomerate. A separation distance of 1.5 nm for the largest agglomerate provides a good qualitative agreement with the experimental data. Thus it will be adopted to calculate the collision efficiency of soot particles and aggregates. Fig. 4 shows the collision efficiency calculated using different Hamaker constant for the soot particles, ranging from 3E − 20 J of benzene to 5E − 19 J of graphite. The Hamaker constant between two different colliding entities is calculated by the geometric average, while for the separation distance the average value is assumed.

The assessment presented above indicated that the following values can be adopted for the separation distance D: 0.21 nm for heavy PAHs (BIN1-4), 1.5 nm for the largest aggregate (BIN25) and the interpolated value between 0.21 and 1.5 proportional to the particle size for the remaining particle and aggregates (BIN5-24). As a result, the collision efficiency between soot particles then increases with the particle size. The collision efficiency of small particles is found to be in the range of 0.1 at room temperature and decreases to ~0.01 at 600 K, while the collision efficiency of large particles approaches unity and is less sensitive to temperature. These results are in reasonable agreement with the observations of Sirignano and D'Anna [21].

4. BSSF flames results and discussions

The numerical simulations of BSSF flames were performed using quasi-one-dimensional simulation and assuming the boundary conditions from the measured temperatures at the burner surface and the stagnation plane. The model is able to reproduce the measured flame structure rather well. The comparison between computed and measured temperature profiles is shown in Fig. 5. The maximum temperature location from the model prediction seems slightly shifted towards the burner, but it is within the experimental uncertainties. The computed temperature profiles are slightly over-predicted in the post-flame region for the large burner-to-stagnation surface separation of flames L3 and L4.

The model for collision efficiency with temperature dependent coefficients discussed above has been included in the soot kinetic mechanism. The reference coagulation rate is $1.6 \times 10^{13} T^{0.5} nC^{1/6}$ cm^3 mol^{-1} s^{-1}, where nC is the number of carbon atoms, and it is used to account for the collision frequency [13]. This

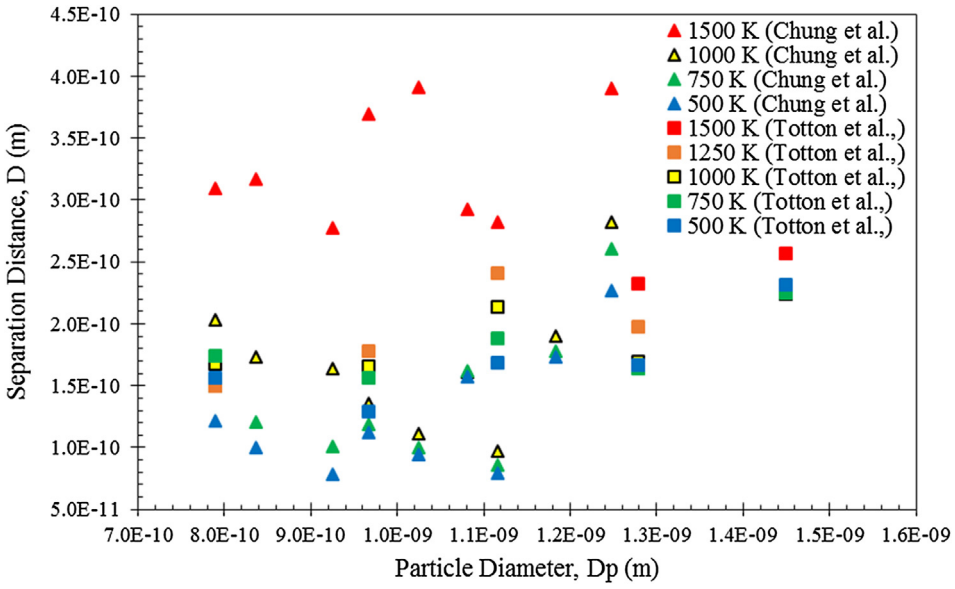

Fig. 2. Calculated separation distance as a function of particle diameter. Triangle: calculated from Chung et al. [22]. Rectangle: calculated from Totton et al. [23]. Different colors represent at various temperatures (red: 1500 K, orange: 1250 K, yellow: 1000 K, green: 750 K and blue: 500 K). (For interpretation of the references to colour in this figure legend, the reader is referred to the web version of this article.)

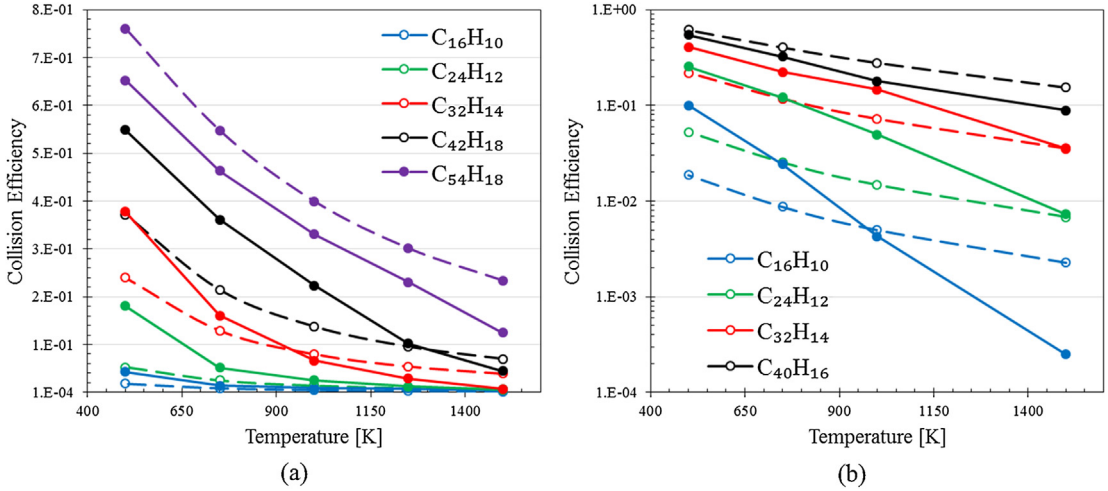

Fig. 3. Comparison of collision efficiency of different PCAHs between collision efficiency used in this work (dashed lines) and the MD results (solid lines) as a function of temperature. Left panel: comparison of collision efficiency with Totton et al. [23]. Right panel: comparison of collision efficiency with Chung et al. [22].

reference coagulation rate is within an order of magnitude difference if compared to the rate proposed rate by Saggese et al. [29], and it is higher by a factor of two than the proposed rate by Sirignano et al. [13].

The comparison between predicted and measured soot PSDFs are shown in Fig. 6. The model prediction fairly agrees with the experimental data except for the young particles (at small burner-to-stagnation plane separation distance), where the model over-predicts the particle sizes. In these conditions, this deviation is related to the contribution of PAH condensation to surface growth. This, in turn, suggests that the model either overestimates the formation of PAH and/or over-predicts the total rate of surface growth reactions, in particular PAH condensation. Despite these deviations, the predicted PSDF of incipient particles, i.e. the nucleation mode, is in general well captured by the model. The prediction of mature soot is in agreement in the low temperature flames, but it is slightly under-predicted at high temperatures. The segregation between the nucleation and coagulation mode experimentally observed is only partially captured by the model, which shows a limited trough at about 10–20 nm. This discrepancy is likely due to a low coagulation rate between soot particles and aggregates. The coagulation rate involving medium and large particle size should be investigated further. Additionally, the definition of particle size in the model is considered as the equivalent spherical diameter, assuming an effective density corresponding to its actual mass, whereas the experimental study measured the mobility diameter using a differential mobility analyzer (DMA). This different definition could lead to some discrepancies especially for aggregates.

Fig. 7 shows the soot volume fraction and number density of particles greater than 2.5 nm as a function of the burner-to-stagnation surface separation. The prediction of soot volume fraction is in generally good agreement with experimental results, although the volume fraction at the smallest burner-to-surface separation is overestimated in all the conditions as can also be seen from their PSDFs. The prediction of number density can be considered acceptable, since the discrepancy is less than one order of magnitude. However, the model is not able to completely reproduce the observed trend with the burner-to-surface separation distance. This difficulty is related to the incomplete prediction of the soot PSDF, which exhibits a deep trough for particle sizes in the range from 10 to 20 nm, which is only partially captured by the model.

Fig. 8 shows the comparison of soot number density and volume fraction between the model proposed in this work, which accounts for the effects of temperature on collision efficiencies, and the model neglecting this temperature dependency. In the last case, the collision efficiencies at two different fixed temperatures of 500 K and 1500 K are

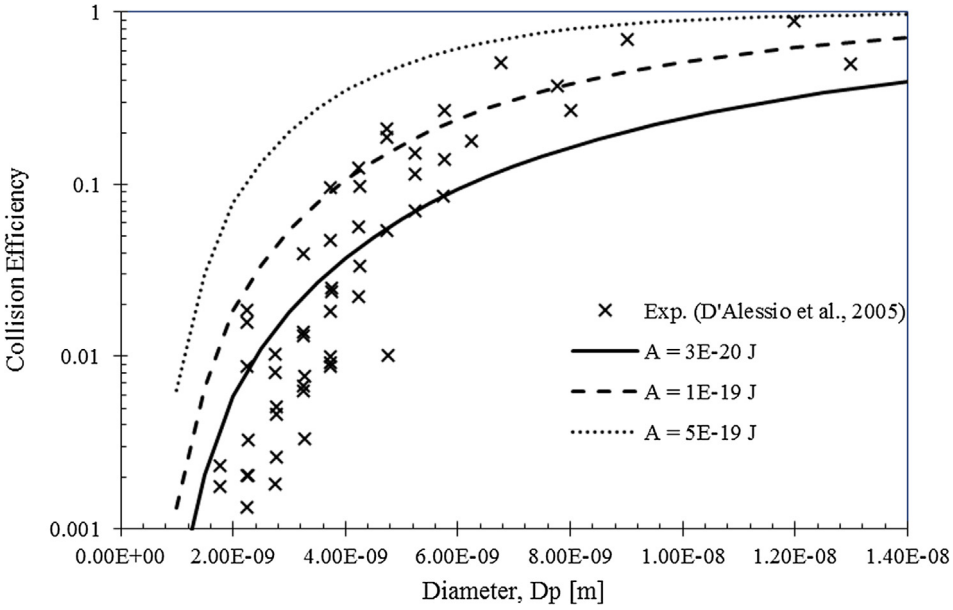

Fig. 4. Comparison of collision efficiency as a function of particle diameter between the observation from D'Alessio et al. [17] (symbol) and the calculated by this work with an Hamaker constant of A = 3E − 20 J (solid line), A = 1E − 19 J (dashed line) and A = 5E − 19 J (dotted line).

assumed. The model results with fixed collision efficiency estimated at 500 K (dashed lines) are influenced by the highest collision efficiencies, which lead to larger particle sizes and soot yields. On the other hand, the model with fixed collision efficiency estimated at 1500 K (dotted lines) provides similar soot volume fraction profiles to the temperature-dependent model. However, lower soot number density is observed because of the lower collision efficiency at high temperatures. The temperature-dependent model is able to better characterize the post-flame region, which has a decreasing temperature. This suggests that the model neglecting temperature is still acceptable if the collision efficiency is taken from appropriate temperature (which may change depending on flame conditions), but the temperature-dependent model

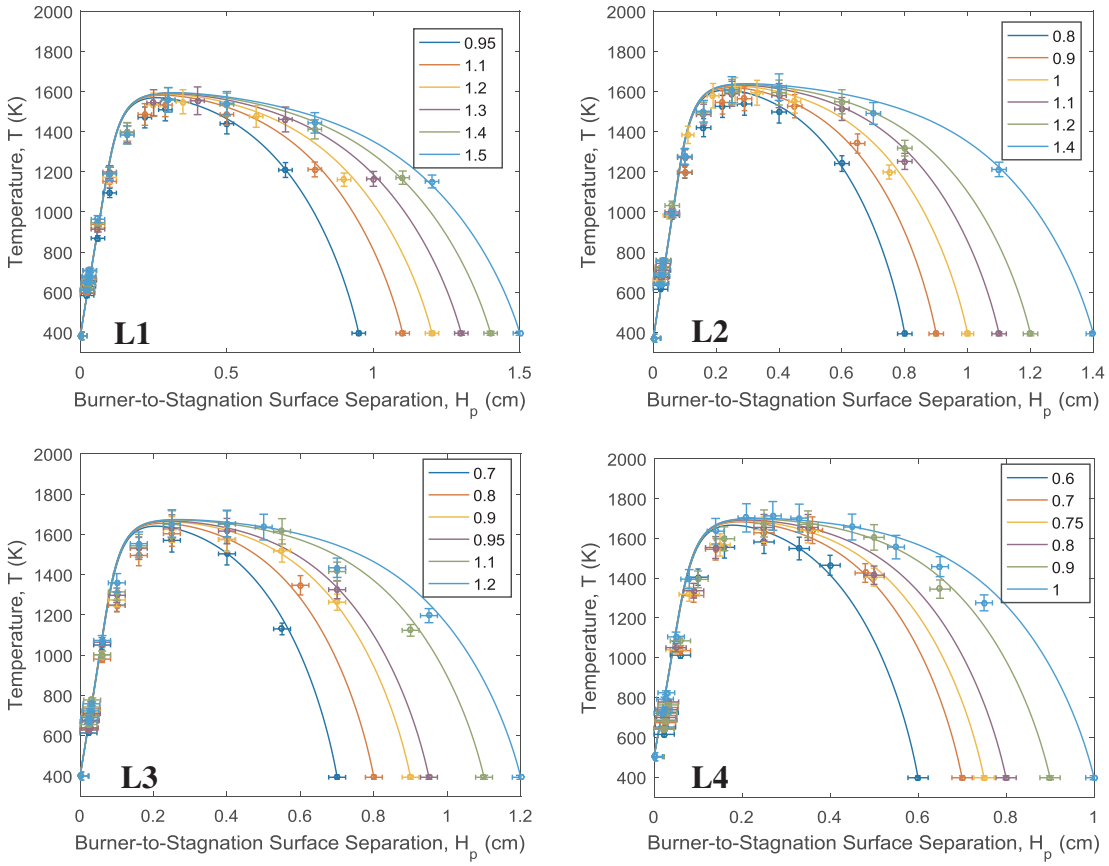

Fig. 5. Comparison between computed (solid lines) and measured (symbols) axial temperature profiles at different burner-to-stagnation surface separation distance. See Table 2 for flame conditions.

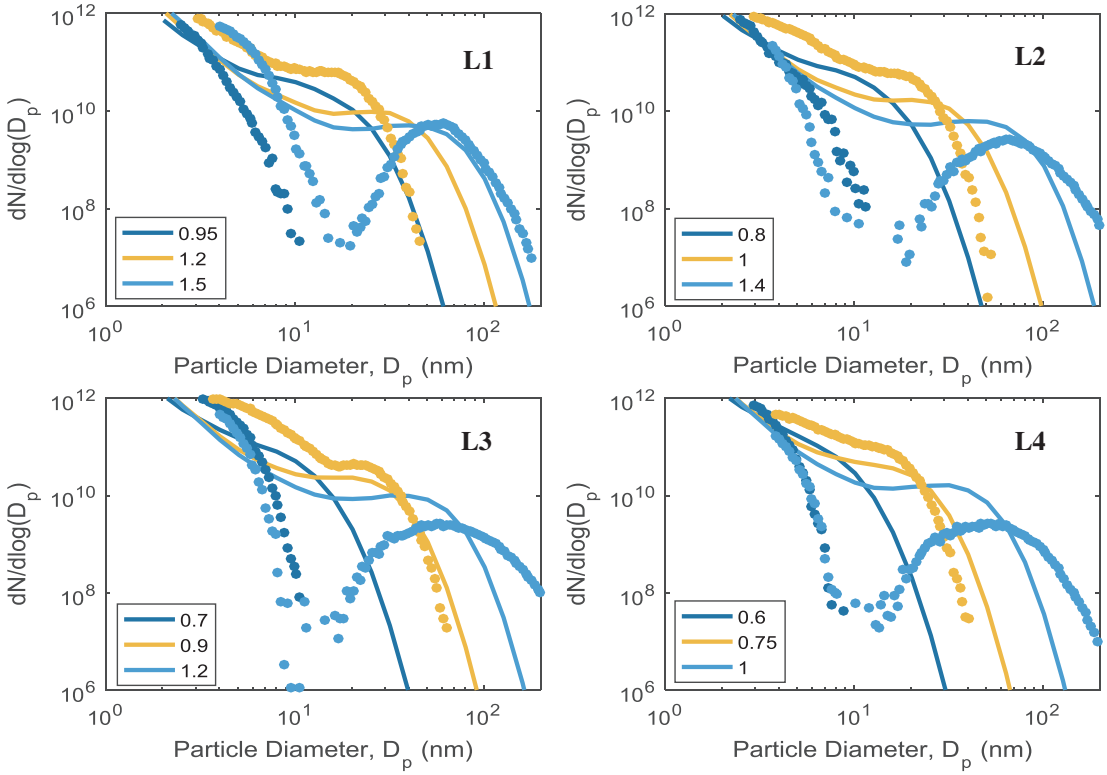

Fig. 6. Comparison between computed (solid lines) and measured (symbols) PSDFs at different burner-to-stagnation surface separation distance. Different colors represent PSDFs at each separation distance (cm).

has a more general validity, especially on soot number density.

5. Conclusions

In this work, a revised discrete sectional model for soot is presented. This kinetic mechanism includes temperature-dependent collision

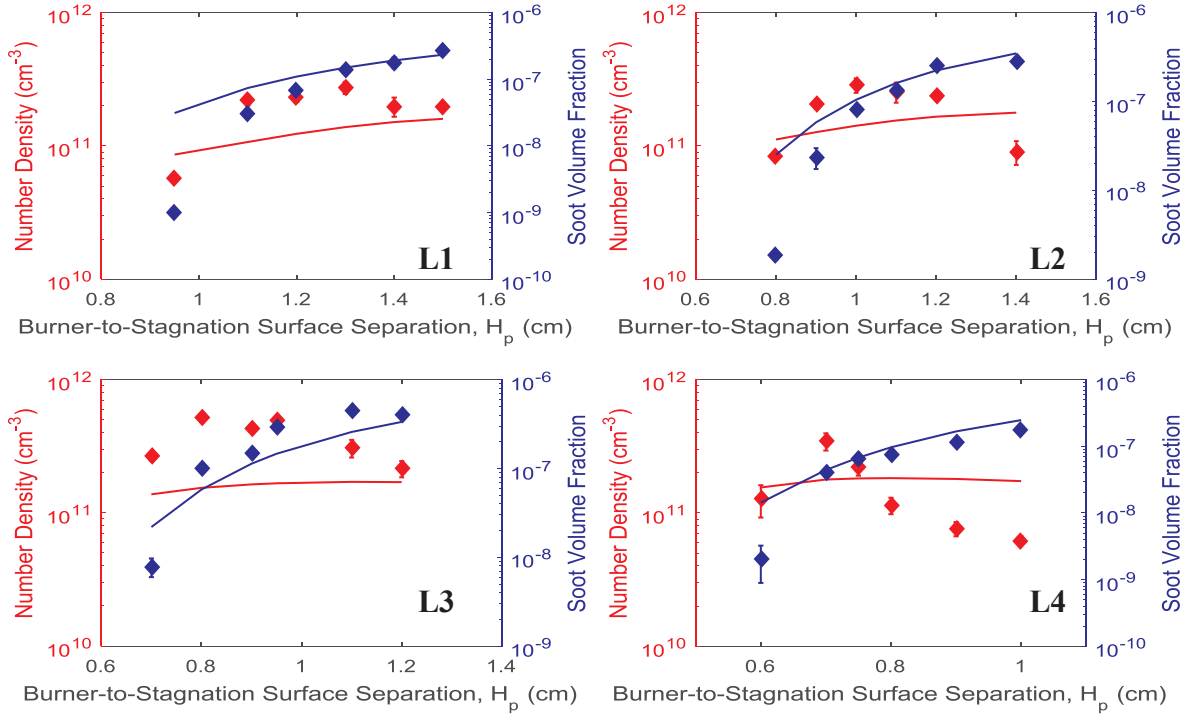

Fig. 7. Comparison between computed (solid lines) and measured (symbols) PSDF at different burner-to-stagnation surface separation distance. Red color indicates soot number density, blue indicates soot volume fraction. (For interpretation of the references to colour in this figure legend, the reader is referred to the web version of this article.)

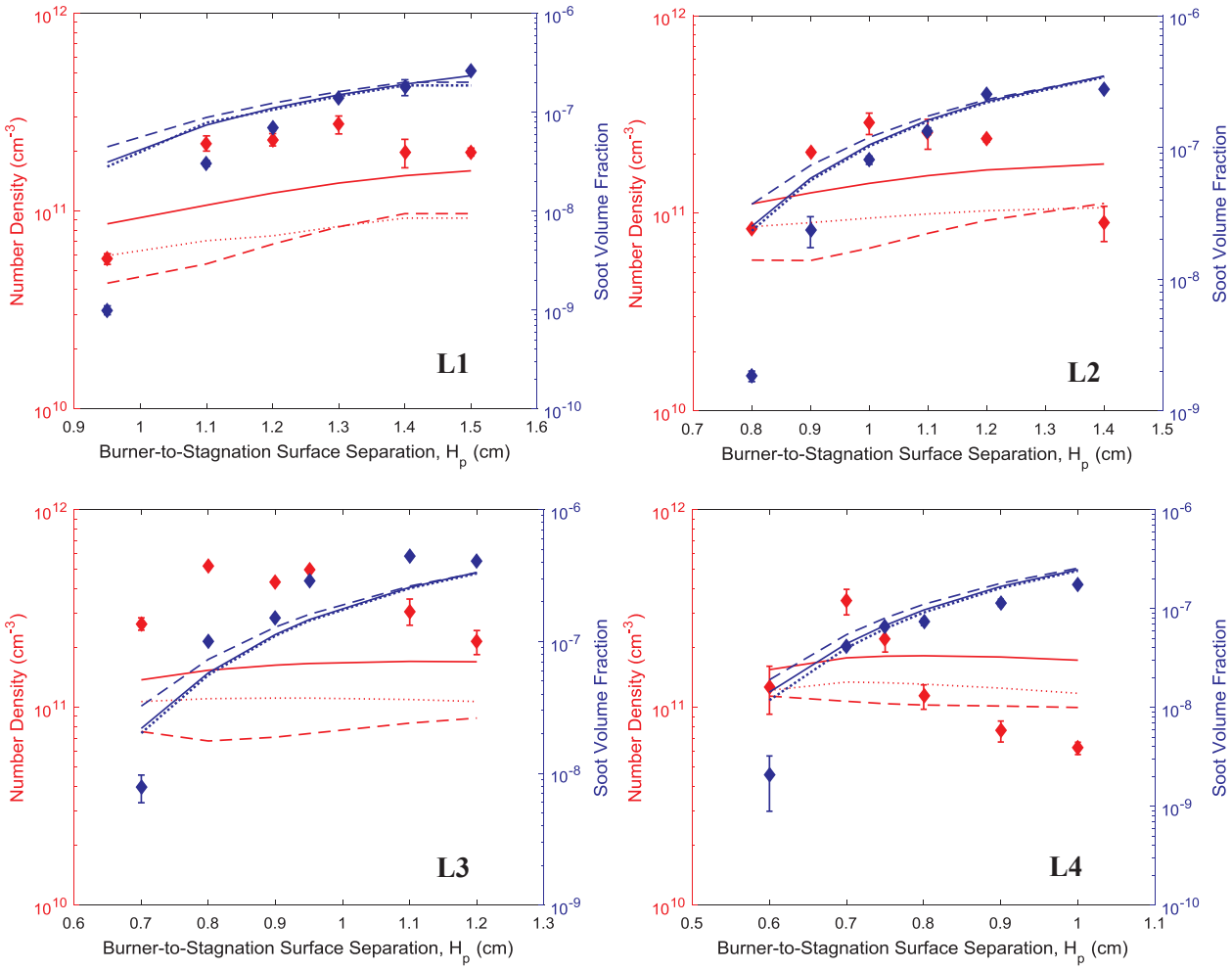

Fig. 8. Comparison of soot number density and volume fraction at different burner-to-stagnation surface separation distance between the temperature-dependent model (solid lines) and the models neglecting the temperature dependency: the model considering collision efficiency at 500 K (dashed lines) and the model considering collision efficiency at 1500 K (dotted lines).

efficiencies for PAH and soot particles and aggregates. The collision efficiency of each particle size range is compared with both available experimental data and molecular dynamics simulations at different temperatures. This comparison showed a good qualitative agreement, and a reasonable quantitative one, especially at high temperatures.

This revised kinetic model was used to simulate several ethylene premixed sooting flames in a wide range of conditions, always assuming the same BSSF configuration. The model successfully predicted the temperature profiles and flame structure in all the flame locations. The computed temperature profiles were slightly overestimated in the post-flame region for the large separations and high temperature cases (flames L3 and L4).

Model predictions obtained using this revised soot model were in satisfactory agreement with soot measurements, although the model over-predicted the particle sizes at the small burner-to-stagnation surface separation, leading to the larger volume fraction of soot. The predicted PSDFs of incipient particles were in reasonable agreement with measurements in all cases. For mature soot, the model prediction captured the low temperature cases (L1 and L2) but slightly underestimated the soot in some cases (L3). Although the model could not fully reproduce the measured PSDF, the overall predictions of soot number density and volume fraction are acceptable. The discrepancy between model predictions and experimental measurements should be investigated further, including PAH formation in rich flames, especially their role in soot growth, and the coagulation rate involving medium and large particle size in order to better characterize the coagulation mode of PSDF. Additionally, the comparison between the temperature-dependent model and the models neglecting the temperature dependency at fixed temperatures is performed. It showed that the temperature-dependent model could improve the predictions of soot number density, which is controlled by small particles.

Acknowledgements

We thank Prof. Stefano Buzzaccaro for helpful discussions. This project has received funding from the European Union's Horizon 2020 research and innovation programme under the Marie Sklodowska-Curie grant agreement No 643134.

References

[1] Bockhorn H, D'Anna A, Sarofim A.F, Wang H. Combustion generated fine carbonaceous particles 2007. doi:10.5445/KSP/1000013744.
[2] Guerreiro C, Gonzalez Ortiz A, de Leeuw F, Viana M, Horalek J. Air quality in Europe — 2016 report 2016. doi:10.2800/413142.
[3] Wang H, Frenklach M. A detailed kinetic modeling study of aromatics formation, growth and oxidation in laminar premixed ethylene and acetylene flames. Combust Flame 1997;2180:173–221.
[4] Frenklach M, Clary DW, Gardiner WC, Stein SE. Detailed kinetic modeling of soot formation in shock-tube pyrolysis of acetylene. Symp Combust 1985;20:887–901. https://doi.org/10.1016/S0082-0784(85)80578-6.
[5] D'Anna A, Kent JH. A model of particulate and species formation applied to laminar, nonpremixed flames for three aliphatic-hydrocarbon fuels. Combust Flame 2008;152:573–87. https://doi.org/10.1016/j.combustflame.2007.08.003.
[6] Wang K, Villano SM, Dean AM. Reactions of allylic radicals that impact molecular

weight growth kinetics. Phys Chem Chem Phys 2015;17:1–28. https://doi.org/10.1039/c4cp05308g.
[7] Colket MB, Seery DJ. Reaction mechanisms for toluene pyrolysis. Symp Combust 1994;25:883–91. https://doi.org/10.1016/S0082-0784(06)80723-X.
[8] Herdman JD, Miller JH. Intermolecular potential calculations for polynuclear aromatic hydrocarbon clusters. J Phys Chem A 2008;112:6249–56. https://doi.org/10.1021/jp800483h.
[9] Miller JA, Klippenstein SJ, Georgievskii Y, Harding LB, Allen WD, Simmonett AC. Reactions between resonance stabilized radicals: Propargyl + Allyl. J Phys Chem A 2010;114:4881–90.
[10] Zhang HB, Hou D, Law CK, You X. Role of carbon-addition and hydrogen-migration reactions in soot surface growth. J Phys Chem A 2016;120:683–9. https://doi.org/10.1021/acs.jpca.5b10306.
[11] Wang H. Formation of nascent soot and other condensed-phase materials in flames. Proc Combust Inst 2011;33:41–67. https://doi.org/10.1016/j.proci.2010.09.009.
[12] Veshkini A, Eaves NA, Dworkin SB, Thomson MJ. Application of PAH-condensation reversibility in modeling soot growth in laminar premixed and nonpremixed flames. Combust Flame 2016;167:335–52. https://doi.org/10.1016/j.combustflame.2016.02.024.
[13] Sirignano M, Kent J, D'Anna A. Modeling formation and oxidation of soot in nonpremixed flames. Energy Fuels 2013;27:2303–15. https://doi.org/10.1021/ef400057r.
[14] Dobbins RA, Fletcher RA, Lu W. Laser microprobe analysis of soot precursor particles and carbonaceous soot. Combust Flame 1995;100:301–9. https://doi.org/10.1016/0010-2180(94)00047-V.
[15] Balthasar M, Frenklach M. Monte-Carlo simulation of soot particle coagulation and aggregation: the effect of a realistic size distribution. Proc Combust Inst 2005;30:1467–75. https://doi.org/10.1016/j.proci.2004.07.035.
[16] Wentzel M, Gorzawski H, Naumann KH, Saathoff H, Weinbruch S. Transmission electron microscopical and aerosol dynamical characterization of soot aerosols. J Aerosol Sci 2003;34:1347–70. https://doi.org/10.1016/S0021-8502(03)00360-4.
[17] D'Alessio A, Barone AC, Cau R, D'Anna A, Minutolo P. Surface deposition and coagulation efficiency of combustion generated nanoparticles in the size range from 1 to 10 nm. Proc Combust Inst 2005;30:2595–603. https://doi.org/10.1016/j.proci.2004.08.267.
[18] Mueller ME, Blanquart G, Pitsch H. Hybrid method of moments for modeling soot formation and growth. Combust Flame 2009;156:1143–55. https://doi.org/10.1016/j.combustflame.2009.01.025.
[19] Yapp EKY, Chen D, Akroyd J, Mosbach S, Kraft M, Camacho J, et al. Numerical simulation and parametric sensitivity study of particle size distributions in a burner-stabilised stagnation flame. Combust Flame 2015;162:2569–81. https://doi.org/10.1016/j.combustflame.2015.03.006.
[20] Eberle C, Gerlinger P, Aigner M. A sectional PAH model with reversible PAH chemistry for CFD soot simulations. Combust Flame 2017;179:63–73. https://doi.org/10.1016/j.combustflame.2017.01.019.
[21] Sirignano M, D'Anna A. Coagulation of combustion generated nanoparticles in low and intermediate temperature regimes: an experimental study. Proc Combust Inst 2013;34:1877–84. https://doi.org/10.1016/j.proci.2012.06.119.
[22] Chung SH, Violi A. Peri-condensed aromatics with aliphatic chains as key intermediates for the nucleation of aromatic hydrocarbons. Proc Combust Inst 2011;33:693–700. https://doi.org/10.1016/j.proci.2010.06.038.
[23] Totton TS, Misquitta AJ, Kraft M. A quantitative study of the clustering of polycyclic aromatic hydrocarbons at high temperatures. Phys Chem Chem Phys 2012;14:4081–94. https://doi.org/10.1039/c2cp23008a.
[24] Mansurov ZA. Soot formation in combustion processes (review). Combust Explos Shock Waves 2005;41:727–44. https://doi.org/10.1007/s10573-005-0083-2.
[25] Abid AD, Tolmachoff ED, Phares DJ, Wang H, Liu Y, Laskin A. Size distribution and morphology of nascent soot in premixed ethylene flames with and without benzene doping. Proc Combust Inst 2009;32:681–8. https://doi.org/10.1016/j.proci.2008.07.023.
[26] Lin H, Gu C, Camacho J, Lin B, Shao C, Li R, et al. Mobility size distributions of soot in premixed propene flames. Combust Flame 2016;172:365–73. https://doi.org/10.1016/j.combustflame.2016.07.002.
[27] Gu C, Lin H, Camacho J, Lin B, Shao C, Li R, et al. Particle size distribution of nascent soot in lightly and heavily sooting premixed ethylene flames. Combust Flame 2016;165:177–87. https://doi.org/10.1016/j.combustflame.2015.12.002.
[28] Tang Q, Cai R, You X, Jiang J. Nascent soot particle size distributions down to 1nm from a laminar premixed burner-stabilized stagnation ethylene flame. Proc Combust Inst 2016. https://doi.org/10.1016/j.proci.2016.08.085.
[29] Saggese C, Ferrario S, Camacho J, Cuoci A, Frassoldati A, Ranzi E, et al. Kinetic modeling of particle size distribution of soot in a premixed burner-stabilized stagnation ethylene flame. Combust Flame 2015;162:3356–69. https://doi.org/10.1016/j.combustflame.2015.06.002.
[30] Saggese C, Frassoldati A, Cuoci A, Faravelli T, Ranzi E. A wide range kinetic modeling study of pyrolysis and oxidation of benzene. Combust Flame 2013;160:1168–90. https://doi.org/10.1016/j.combustflame.2013.02.013.
[31] Ranzi E, Frassoldati A, Grana R, Cuoci A, Faravelli T, Kelley AP, Law CK. Hierarchical and comparative kinetic modeling of laminar flame speeds of hydrocarbon and oxygenated fuels. Prog Energy Combust Sci 2012;38:468–501. https://doi.org/10.1016/j.pecs.2012.03.004.
[32] Cuoci A, Frassoldati A, Faravelli T, Ranzi E. OpenSMOKE++: an object-oriented framework for the numerical modeling of reactive systems with detailed kinetic mechanisms. Comput Phys Commun 2015;192:237–64. https://doi.org/10.1016/j.cpc.2015.02.014.
[33] Grosshandler WL. RADCAL: a narrow-band model for radiation calculations in a combustion environment. NIST Tech Note 1993;1402.
[34] Sazhin S. An approximation for the absorption coefficient of soot in a radiating gas. Fluent Eur Ltd.; 1994.
[35] Saggese C, Cuoci A, Frassoldati A, Ferrario S, Camacho J, Wang H, et al. Probe effects in soot sampling from a burner-stabilized stagnation flame. Combust Flame 2016;167:184–97. https://doi.org/10.1016/j.combustflame.2016.02.013.
[36] Saffaripour M, Veshkini A, Kholghy M, Thomson MJ. Experimental investigation and detailed modeling of soot aggregate formation and size distribution in laminar coflow diffusion flames of Jet A-1, a synthetic kerosene, and n-decane. Combust Flame 2014;161:848–63. https://doi.org/10.1016/j.combustflame.2013.10.016.
[37] Frenklach M, Wang H. Detailed mechanism and modeling of soot particle formation. Soot Form Combust 1994:165–92. https://doi.org/10.1007/978-3-642-85167-4_10.